Chinese Chemical Letters 34 (2023) 107328

Contents lists available at ScienceDirect

Chinese Chemical Letters

journal homepage: www.elsevier.com/locate/cclet

Bimetallic $CoNiSe_2$/C nanosphere anodes derived from Ni-Co-metal-organic framework precursor towards higher lithium storage capacity

Weifan Zhang[a,c], Lei Wang[a,c], Guochun Ding[a,c], Yuejia Yang[a,c], Guang Yang[a,c], Jing Xu[a,c], Ningning Xu[a,c], Lingling Xie[b,c], Qing Han[a,c], Limin Zhu[a,c,*], Xiaoyu Cao[a,c,*], Jianmin Ma[d,**]

[a] School of Chemistry and Chemical Engineering, Henan University of Technology, Zhengzhou 450001, China
[b] School of Environmental Engineering, Henan University of Technology, Zhengzhou 450001, China
[c] Key Laboratory of High Specific Energy Materials for Electrochemical Power Sources of Zhengzhou City, Henan University of Technology, Zhengzhou 450001, China
[d] School of Materials and Energy, University of Electronic Science and Technology of China, Chengdu 611731, China

ARTICLE INFO

Article history:
Received 19 December 2021
Revised 5 January 2022
Accepted 10 March 2022
Available online 14 March 2022

Keywords:
MOFs
Bimetallic compound
$CoNiSe_2$/C anode nanosphere
Lithium-ion batteries
Lithium storage performance

ABSTRACT

Through uncomplicated carbonation process, a carbon-embedded $CoNiSe_2$/C nanosphere was synthesized from Ni-Co-MOF (metal-organic framework) precursor whose controllable structure and synergistic effect of bimetallic Ni/Co brought $CoNiSe_2$/C anodes with high specific surface area (172.79 m^2/g) and outstanding electrochemical performance. $CoNiSe_2$/C anodes obtained reversible discharge capacities of 850.9 mAh/g at 0.1 A/g after cycling for 100 cycles. In addition, $CoNiSe_2$/C exhibits excellent cycle stability and reversibility in the rate test at a current density of 0.1–2.0 A/g. When the current density returns to 0.5 A/g for 150 cycles, its discharge ratio the capacity is 330.8 mAh/g. Electrochemical impedance spectroscopy (EIS) tests suggested that $CoNiSe_2$/C anodes had a lower charge transfer impedance of 130.02 Ω after 30 cycles. *In-situ* X-ray diffraction (XRD) tests confirmed the alloying mechanism of $CoNiSe_2$/C which realized higher lithium storage capacity. This work affords substantial evidence for the extension of bimetallic selenides in secondary batteries, promoting the development of bimetallic selenides in anode materials for LIBs.

Recently, transition metal selenides become popular as anodes in lithium-ion batteries (LIBs) by reason of high capacity in theory and controllable morphology. There is no doubt that lithium-ion batteries (LIBs) are critical devices to store energy depending on their high energy density, long life and practical convenience [1–3]. Nevertheless, commercial graphite anodes with low theoretical lithium-embedded capacity (372 mAh/g) could not satisfy enormous energy demands [4–7]. Higher theoretical capacity of Ni and Co based compounds, such as Co_3O_4 [8], Co_9S_8 [9], NiS [10], NiS_2 [11] and Mn_2O_3 [12] are regarded as new-generation high-performance alternative anodes. Unfortunately, drastic structural changes of above materials during charging and discharging leading to high irreversible capacity loss and rapid capacity decay is a great challenge for further development in LIBs [13–15]. As a consequence, nanomaterials with clear internal hollow structure were designed to effectively avoid the agglomeration and fragmentation of active substances during cycles [16–18].

At the same time, transition metal oxides, sulfides and selenides with high specific capacity in theory have become hotspot [19–21]. Particularly, metal selenides possess higher ionic conductivity and better electrochemical activity than metal sulfides and metal oxides [22]. In addition, selenium-based materials with low band gap and high covalent state speed up electron transmission and improve the conductivity of battery [23,24]. The NiSe/C nanoflower synthesized by Wang's group released higher initial discharge capacity of 1688.4 mAh/g [25]. Wang's group also proposed the $CoSe_2$/CNT nanosheet displaying better electrochemical performance [26]. Compared with monometallic selenides, bimetallic selenides are equipped with better synergistic effect and more electron reaction processes, obtaining excellent electrochemical activity and redox reversibility [27,28]. The Ni-Co-Se@C composite synthesized by Yang's group released a reversible discharge

* Corresponding authors at: School of Chemistry and Chemical Engineering, Henan University of Technology, Zhengzhou 450001, China.
** Corresponding author.
E-mail addresses: lmzhu@haut.edu.cn (L. Zhu), caoxy@haut.edu.cn (X. Cao), nanoelechem@uestc.edu.cn (J. Ma).

https://doi.org/10.1016/j.cclet.2022.03.051
1001-8417/

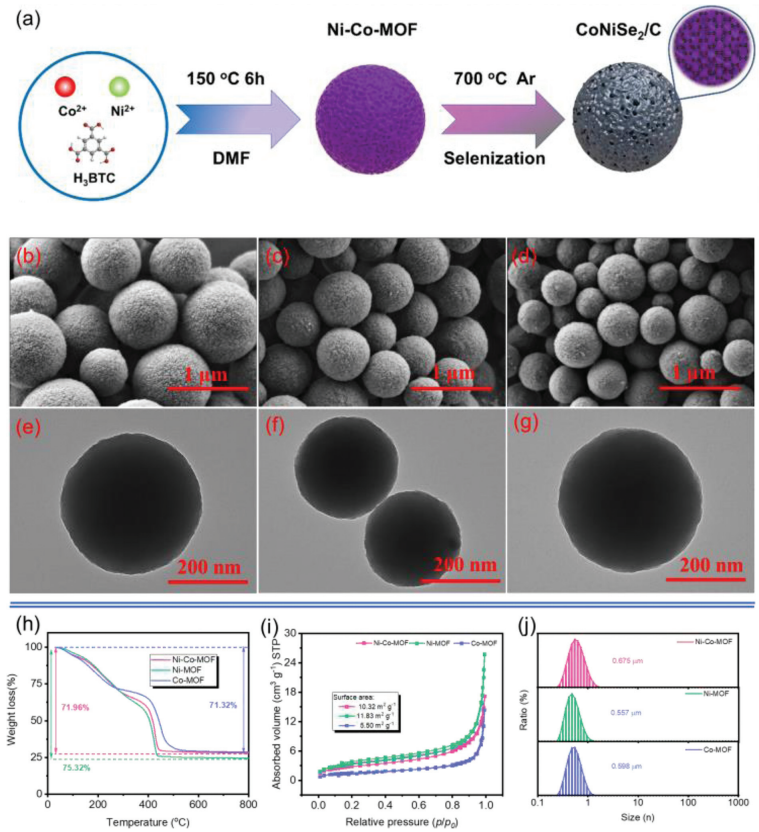

Fig. 1. (a) Synthetic schematic diagram of $CoNiSe_2$/C nanosphere. SEM (b–d) and TEM (e–g) images of Ni-Co-MOF, Ni-MOF and Co-MOF. (h) Thermogravimetric analysis curves of precursors, (i) N_2 adsorption isotherm curves and (j) particle size distribution of Ni-Co-MOF, Ni-MOF and Co-MOF.

capacity of 2061 mAh/g [29]. It is of great essence to employ selenium-based materials as high-performance LIBs' anode because their research is still less after solving the problem of huge volume during cycle [30–32], and the lithium storage mechanism of selenium-based anodes also needs in-depth study.

Metal-organic framework materials (MOFs) are the most widely sacrificial templates due to the large specific surface area, porosity and controllable structure [33–35]. For example, CoS_2/NC/S from Co-MOF sacrifice template [36], Co-MOF-74@MWCNT from Co-MOF-74 precursor [37] and C/Si/ZIF-8 as LIBs anodes showed excellent electrochemical performance [38]. However, MOF materials have lower conductivity [39], carbon materials need to be added, which can inhibit the volume expansion of substances during cycle apart from the improved conductivity [40,41].

Here, three nanosphere materials, named $CoNiSe_2$/C, NiSe/C and $CoSe_2$/C composites were synthesized by simple solvothermal method *via* the selenylation of Ni-Co-MOF, Ni-MOF and Co-MOF. These composites all inherited original nanosphere morphologies. By comparison of physical properties, electrochemical performance, lithium storage mechanisms and kinetic characteristics of these composites, the $CoNiSe_2$/C had better electrochemical performance than the monometallic NiSe/C and $CoSe_2$/C. After $CoNiSe_2$/C nanospheres are cycled for 150 weeks in the rate test under 0.1–2.0 A/g, the stable discharge capacity is 330.8 mAh/g, and the coulombic efficiency is higher than 98%. Such higher capacity retention and excellent cyclic performance further confirmed the superiority of $CoNiSe_2$/C materials as high-performance LIBs' anodes.

Further purification of the purchased chemical reagents was not implemented and the reagents were directly used. Ni-Co-MOF nanosphere precursor was synthesized by hydrothermal method as follow. Firstly, $Ni(NO_3)_2{\cdot}6H_2O$ (4 mmol, 1.454 g) and $Co(NO_3)_2{\cdot}6H_2O$ (2 mmol, 1.455 g) powders were added in *N*,*N*-dimethylformamide (DMF, 60 mL) solution with magnetic stir. Then, 2.0 g polyvinylpyrrolidone (PVP) powder was dissolved in above solution until its complete dissolution followed by 0.3 g 1,3,5-benzenetricarboxylic acid (H_3BTC). Subsequently, the polytetrafluoroethylene reaction containing above mixed solution was heated for 6 h at 150 °C. The obtained product was rinsed with DMF and ethanol, and was vacuum dehydrated at 70 °C overnight to obtain pink solid. Ni-MOF and Co-MOF precursors were synthesized using the same procedure except the absence of $Co(NO_3)_2{\cdot}6H_2O$ powder or $Ni(NO_3)_2{\cdot}6H_2O$ powder.

At last, Ni-Co-MOF, Ni-MOF and Co-MOF precursors were calcined to 700 °C (5 °C/min) for 2 h at argon atmosphere with Se powder at a blending ratio of 1:3. The final black powders were denoted as $CoNiSe_2$/C, NiSe/C and $CoSe_2$/C, respectively.

Fig. 1a simplified the synthesis process of $CoNiSe_2$/C. The Ni-Co-MOF precursor was directly synthesized by solvothermal method and directly subjected to high-temperature calcination. Carbonization produces a carbon-coated $CoNiSe_2$/C nanosphere composite material during selenization process.

The phase features and structures of three composites were conducted by powder X-ray diffractometer (XRD) and Raman spectra. The particle size, specific surface area, pore size distribution and void volume were investigated by laser particle size analyzer (LPSA) and Brunauer-Emmett-Teller (BET). In addition, the surface configuration and internal microstructures were tested by SEM and TEM. The high-resolution TEM (HRTEM) containing selected-area diffraction (SAED) images was studied to further ascertain the lattice composition of composites. The thermal decomposition course and stability of three precursors were carried out by thermogravimetric analysis (TGA) in N_2 atmosphere rom room temperature to

800 °C (10 °C/min). The chemical composition of three composites, valence state and relative content were used by X-ray photoelectron spectroscopy (XPS) tests. At last, *in-situ* XRD tests were performed to confirm the reaction mechanism of $CoNiSe_2$/C.

Anode electrodes (7:1.5:1.5) onto a copper foil included $CoNiSe_2$/C (or NiSe/C, $CoSe_2$/C), Ketjen black (KB), poly(vinylidene fluoride) (PVDF) in NMP. CR2016-type coin cells were finished in an argon-filled glove box using Li metal as anode by adding a mixed electrolyte of 1 mol/L $LiPF_6$ in ethylene carbonate (EC) and dimethyl carbonate (DEC) (EC:DEC = 1:1, v/v). The mass loading was 0.59 mg/cm^2 with a thickness of ~3.5 μm.

Different from the above half-cell assembly method, $LiFePO_4$ was cathode for the assembly of full battery, and the anode was $CoNiSe_2$/C material. The battery devices used are unchanged, and the assembly sequence is adjusted slightly to successfully assemble the full battery.

The SEM and TEM images of Ni-Co-MOF, Ni-MOF and Co-MOF were shown in Figs. 1b–g. Three MOF precursors presented nanosphere structure with similar size and smooth surface (Figs. 1b–d). TEM images showed that the diameter of Ni-Co-MOF was approximately 500 nm without impurities and attached particles (Figs. 1e–g), providing very favorable morphologies and structures for subsequent derived materials. According to the three processes of TG curves, including the volatilization of solvents from 25 °C to 300 °C, the gradual decomposition of part of ligands at 400 °C and a stationary phase after 520 °C, the calcination temperatures of three precursors were 700 °C (Fig. 1h). The nitrogen adsorption/desorption curves in Fig. 1i showed that all the curves belong to II isotherm of H3 type hysteresis ring according to IUPAC classification, suggesting that three MOF precursors had macroporous structure [42]. The specific surface areas are 10.32, 11.83 and 5.50 m^2/g, respectively. The particle size distribution in Fig. 1j showed sizes of Ni-Co-MOF, Ni-MOF and Co-MOF were 0.675, 0.557 and 0.598 μm in average.

Fig. 2a and Figs. S3a and b (Supporting information) were the SEM images of $CoNiSe_2$/C, NiSe/C and $CoSe_2$/C composites. Irregular attached nanoparticles on the surface of nanospheres arose from the decomposition or destruction of MOF precursor during calcination. However, the $CoNiSe_2$/C composite material better inherits the nanosphere structure of the Ni-Co-MOF precursor, showing fewer decomposed particles and a uniform shape. The TEM images of a single nanosphere (Figs. 2b and c, Figs. S3c and d in Supporting information) clearly show that nanoparticles of different sizes are embedded in the matrix of nanospheres, and the particles have different degrees of dispersion due to the higher calcination temperature. HRTEM images clearly manifested the composition and distribution of $CoNiSe_2$/C, NiSe/C and $CoSe_2$/C composites (Fig. 2d and Fig. S3f in Supporting information). The selected lattice fringe of 0.185 nm was well matched with the crystal planes (110) of $CoNiSe_2$/C. According to their SEAD images (Fig. 2e and Fig. S3h in Supporting information), three composites were polycrystalline materials. Fig. 2f and Fig. S4b (Supporting information) showed the mapping and EDS images of $CoNiSe_2$/C, NiSe/C and $CoSe_2$/C composites. Ni, Co and Se elements of $CoNiSe_2$/C were evenly distributed in the selected area. EDS images also revealed the characteristic peaks of every element, agreeing with the XPS results. All the above results affirmed the successful synthesis of three composites.

$CoNiSe_2$/C, NiSe/C and $CoSe_2$/C composites exhibited higher crystallinity according to the strength and smoothness of diffraction peaks in their XRD patterns, well indexed with PDF #65-7038, PDF #75-0610 and PDF #89-2002 standard cards (Fig. 2g). It can be seen that the peak position values of CoNiSe2/C and NiSe/C are relatively close, and the diffraction peaks of CoNiSe2/C 2θ at approximately 32.93°, 44.41° and 49.98°; the diffraction peaks of NiSe/C 2θ at approximately 32.84°, 44.37° and 49.78° are all corresponding to three different crystal planes (101), (102) and (110). The unobserved carbon diffraction peaks were concealed by the strong intensity of diffraction peaks of three composites. No other impurity peaks suggested the successful synthesis with high purity [43]. According to the Roman spectra (Fig. 2h), a D peak (amorphous carbon) at 1307 cm^{-1} and G peak (graphitic carbon) at 1570 cm^{-1} appeared in three spectra, confirming the existence of carbon in composites [44]. The lower peak intensities (I_D/I_G) for $CoNiSe_2$/C (0.54) than NiSe/C and $CoSe_2$/C (0.73, 0.71) suggested that $CoNiSe_2$/C composite had a larger degree of graphitization and less defects, favorably enabling the transfer rate of ions during cycle [45]. The LPSA tests in Fig. 2i showed that the average particle sizes for $CoNiSe_2$/C, NiSe/C and $CoSe_2$/C were 1.3 μm, 51.2 μm and 57.4 μm, respectively. According to the IUPAC classification, three curves belonged to IV-type isotherm with H4 type hysteresis hoops, implying the abundant meso– or microporous structures for three nanospheres [46]. The BET calculation in Fig. 2j showed that the specific surface areas for $CoNiSe_2$/C, NiSe/C and $CoSe_2$/C were 172.79, 224.27 and 194.69 m^2/g, respectively. Lower peak intensity, porous structure and larger specific surface area offers ample active channels for ion transfer and tamps the electrolyte infiltration [47]. The size distribution curves in Fig. S1b (Supporting information) indicated that three composites had microporous and mesoporous structures.

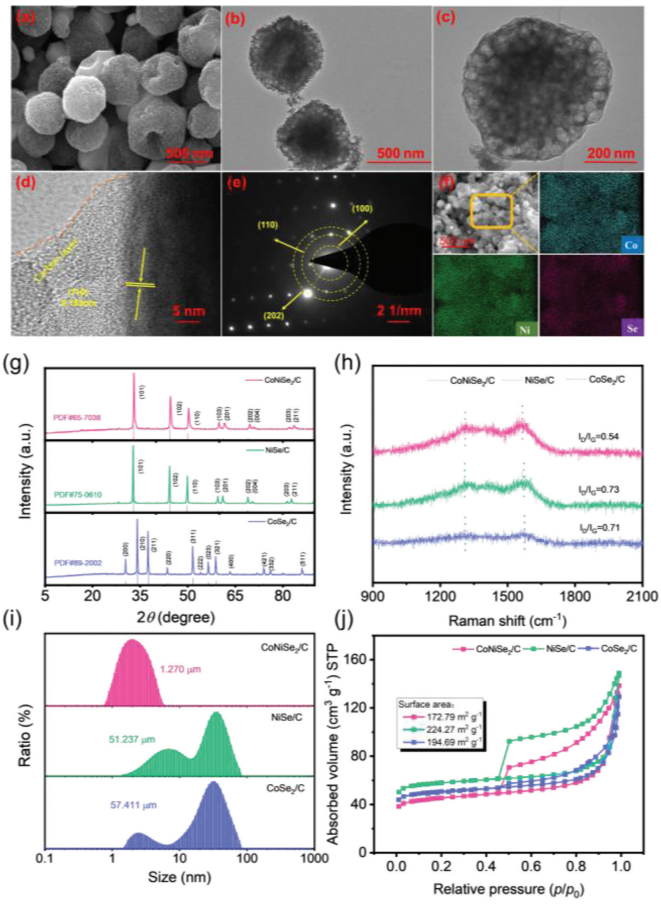

Fig. 2. (a) SEM image, (b, c) TEM images, (d) HRTEM image, (e) SAED image and (f) mapping images of $CoNiSe_2$/C. (g) XRD patterns, (h) Raman spectra, (i) particle size distribution and (j) N_2 adsorption isotherm of $CoNiSe_2$/C, NiSe/C and $CoSe_2$/C.

Fig. 3 showed the XPS spectra of $CoNiSe_2$/C, NiSe/C and $CoSe_2$/C. In the full spectra (Fig. 3a), an obvious peak of O 1s located at 531.9 eV, arising from the absorbed oxygen in air [48]. The existing oxygen also resulted in three characteristic peaks in C 1s spectra

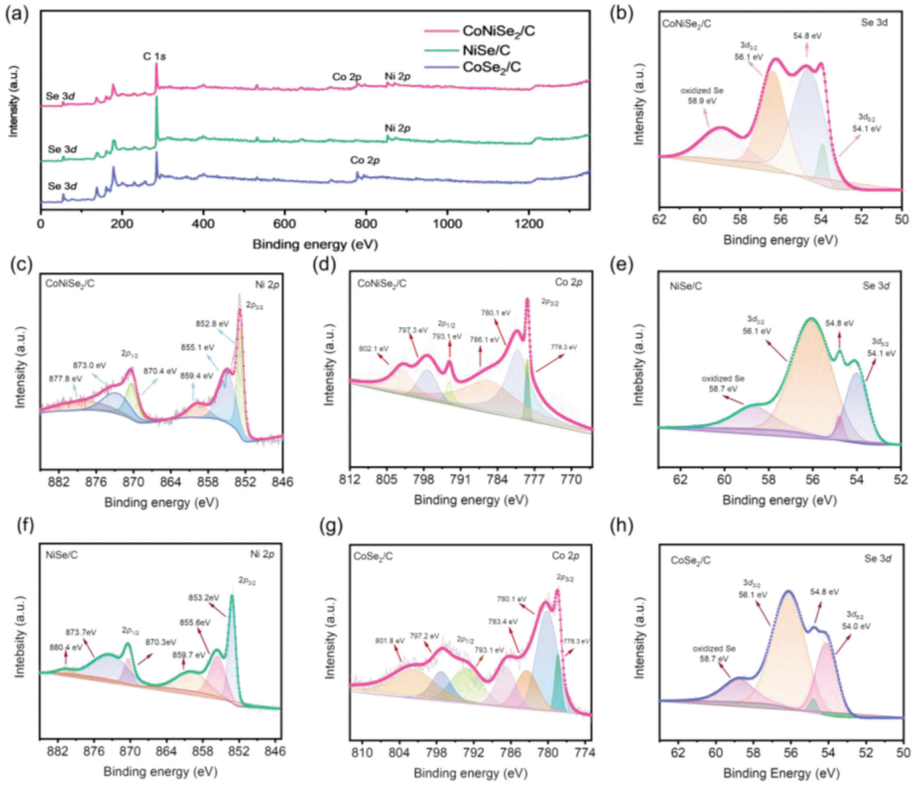

Fig. 3. (a) Full XPS spectra of $CoNiSe_2$/C, NiSe/C and $CoSe_2$/C. (c, f) Ni 2p XPS spectra of $CoNiSe_2$/C and NiSe/C. (d, g) Co 2p XPS spectra of $CoNiSe_2$/C and $CoSe_2$/C. Se 3d XPS spectra of (b) $CoNiSe_2$/C, (e) NiSe/C and (h) $CoSe_2$/C.

(Figs. S2a–c in Supporting information), including C-O, C=O and O-C=O groups [49]. Figs. 3c, d, f and g showed the XPS spectra of Ni and Co element whose 2p peaks were split into two peaks of $2p_{1/2}$ and $2p_{1/3}$. In addition to Ni^{3+}/Ni^{2+} and Co^{3+}/Co^{2+} valence state, Ni^0 and Co^0 state also existed in the composites [50,51]. In the XPS spectra of Se element (Figs. 3b, e and h), the Se 3d peaks were deconvoluted into $3d_{3/2}$ and $3d_{5/2}$ peaks located at 56.1 and 54.0 eV for all composites. Other peaks, called oxidization characteristic peaks, maybe result from the oxidized substances or oxygen-absorbed substances [52].

Figs. 4a–c showed the CV curves of $CoNiSe_2$/C, NiSe/C and $CoSe_2$/C composites at 0.1 mV/s between 0.01–3.0 V. An initial reduction peak at 0.6 V for three composites was related to the solid electrolyte interphase (SEI) or other side reactions [53]. The charge/discharge process of $CoNiSe_2$/C could be described by Eq. 1. A reduction peak at 1.18 V in the first cycle shifted to 1.4 V and 1.6 V in the following cycles, representing the insertion of Li^+ and the transfer of $CoNiSe_2$. The oxidization peak at 2.07 V was related with the formation of $CoNiSe_2$ and Li^+ between Ni, Co and Li_2Se. The charge/discharge processes of NiSe/C and $CoSe_2$/C could be described by Eqs. 2 and 3, whose Li storage mechanisms were similar to that of $CoNiSe_2$ [54], according to related reports the mechanisms are all transformation reactions. The shift to higher redox peaks after first cycle for three materials may be caused by the structure change during the Li^+ insertion/de-insertion process [55]. The highly overlapped CV curves reflect superior redox reversibility, in great consistency with the charge/discharge curves (Figs. 4d–f). As shown in Fig. 4g, the initial charge/discharge capacities for $CoNiSe_2$/C, NiSe/C and $CoSe_2$/C were 1321.2/2207.6, 485.2/970 and 655.5/1352.6 mAh/g at 0.1 A/g. Fig. S6a–c (Supporting information) showed the 30-cycle SEM images of three composites. $CoNiSe_2$/C still maintained original nanosphere structure wrapped by PVDF and KB. This stable structure may be the reason for the ever-rising capacity in the following cycles. However, two monometallic composites assumed collapsed sheet structure because of volume shrinkage during cycle. In addition, Fig. 4h also shows the better rate performance of $CoNiSe_2$/C. The reversible discharge specific capacity at a current density of 0.1–1.0 A/g is 722.6, 620.1, 507.4, 427.7 and 339.1 mAh/g. When the current density returns to 0.1 A/g, due to the pseudocapacitance behavior and the Li^+ activation process, the specific discharge capacity of the two materials has increased to varying degrees [56]. When the current density reaches 0.5 A/g, the reversible capacity of $CoNiSe_2$/C reaches 429.0 mAh/g. Through the charge and discharge platform of $CoNiSe_2$/C in Fig. 4i, it maintains a clear and similar curve, which proves that it has excellent electrochemical stability under different current densities. In addition, the voltage plateau length of $CoNiSe_2$/C gradually decreases with the increase of current density, which is related to the enhanced polarization phenomenon during the cycle. The synergistic effect between bimetal of Ni and Co and carbon promoted the structural stability, and the conductivity was enhanced by Se element [57].

$$CoNi(Se)_2 + 4Li^+ + 4e^- \leftrightarrow Ni + Co + 2Li_2Se \quad (1)$$

$$NiSe + 2Li^+ + 2e^- \leftrightarrow Ni + Li_2Se \quad (2)$$

$$CoNi(Se)_2 + 4Li^+ + 4e^- \leftrightarrow Co + 2Li_2Se \quad (3)$$

Fig. 5a and Table S1 (Supporting information) showed the rate performance of $CoNiSe_2$/C, NiSe/C and $CoSe_2$/C composites. At 0.1, 0.2, 0.5, 0.8, 1.0 and 2.0 A/g, $CoNiSe_2$/C exhibited higher discharge capacities of 813.7, 705.9, 585.9, 482, 394.6 and 259.5 mAh/g, respectively. The carbon coating in $CoNiSe_2$/C anode provides strong conditions for electrolyte penetration and shortens the transmission path of Li^+ ions. While the current rate reverted to 0.5 A/g, $CoNiSe_2$/C obtained the discharge capacity of 332.3 mAh/g, a

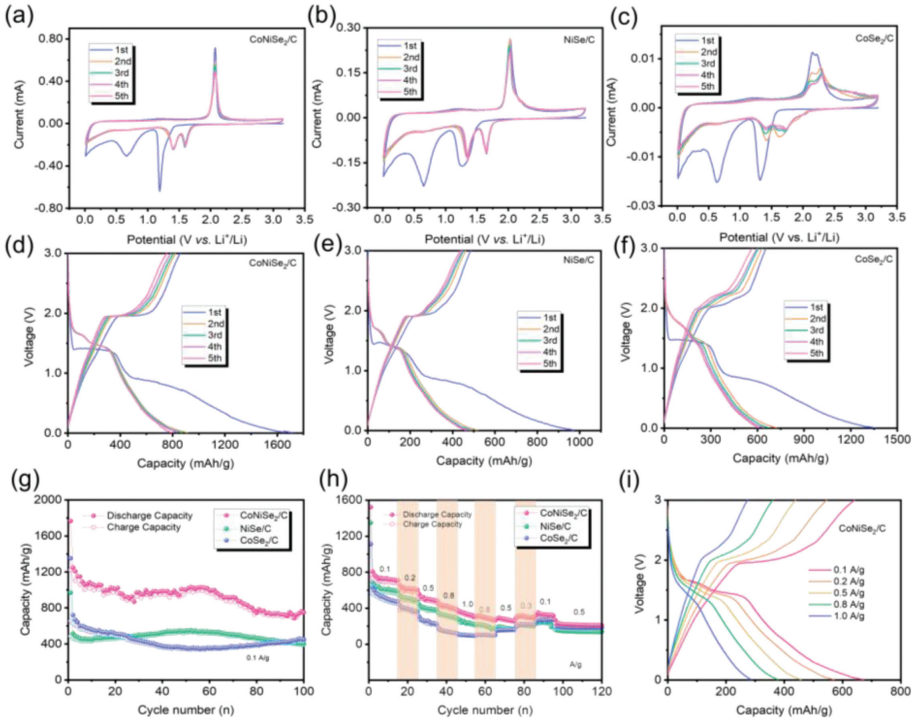

Fig. 4. (a–c) CV curves of $CoNiSe_2$/C, NiSe/C and $CoSe_2$/C at 0.1 mV/s. (d–f) Discharge/charge curves of $CoNiSe_2$/C, NiSe/C and $CoSe_2$/C in the first five cycles. (g) Cyclic performance of $CoNiSe_2$/C, NiSe/C and $CoSe_2$/C at 0.1 A/g for 100 cycles. (h, i) $CoNiSe_2$/C, NiSe/C and $CoSe_2$/C rate performance test chart and corresponding charge-discharge curve under 0.1–1.0 A/g current density.

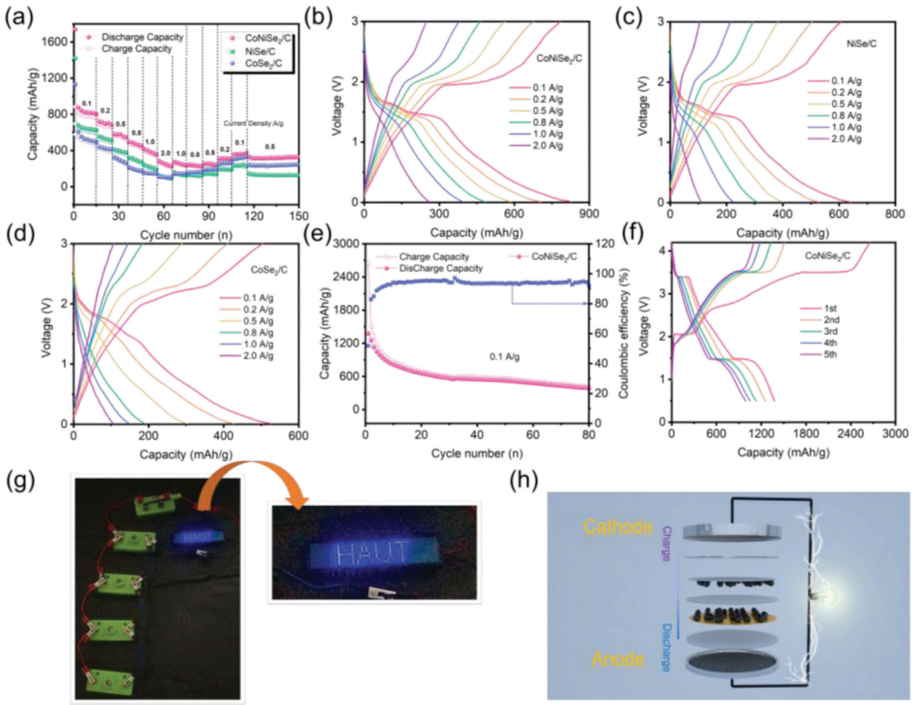

Fig. 5. (a–d) The rate performance test chart and corresponding charge/discharge curves of $CoNiSe_2$/C, NiSe/C and $CoSe_2$/C. (e) Constant current cycle test chart of full battery composed of $CoNiSe_2$/C and $LiFePO_4$. (f) Corresponding charge and discharge curve of $CoNiSe_2$/C full battery cycle test. (g) Schematic diagram of full battery lighting LED lights. (h) Schematic diagram of full battery assembly.

capacity towering over 247.1 and 128.7 mAh/g for NiSe/C and $CoSe_2$/C. Compared with the monometallic and bimetallic chalcogenide reports in Table S2 (Supporting information), the prepared NiSe/C, $CoSe_2$/C and $CoNiSe_2$/C electrodes showed excellent electrochemical performance. In view of their charge/discharge curves related with current density at different levels (Figs. 5b–d), the polarization caused the reduced discharge plateau and increased charge plateau with the current density increasing. The commercial $LiFePO_4$ material was chosen as cathodes and $CoNiSe_2$/C as anodes to construct a full battery (Fig. 5h). At 0.1 A/g between 0.5 and 4.2 V, the full cell obtained an initial charge/discharge capacity of 2656.5/1378.2 mAh/g, which was retained at 379.8/377.4 mAh/g

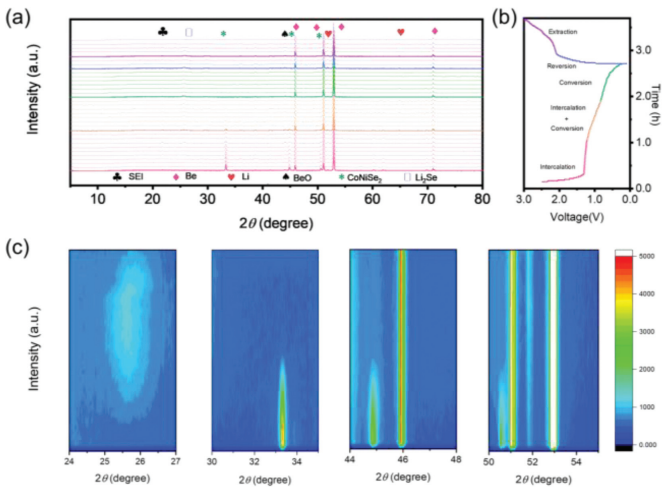

Fig. 6. (a) *In-situ* XRD pattern of $CoNiSe_2$/C of the initial cycle. (b) Corresponding charge/discharge curve and (c) *in-situ* XRD 2θ area details.

with almost 100% Coulombic efficiency after 80 cycles (Fig. 5e). In addition, the working plateau was stable around 3.5 V (Fig. 5f). In a lightened LED experiment (Fig. 5g), four series-wound full cells lightened a LED screen for 3 min.

Fig. 6 showed the *in-situ* XRD analysis of $CoNiSe_2$/C composite to in-depth classify its Li storage mechanism. Window materials including Be (JCPDS No. 72-2381), BeO (JCPDS No. 78-1553) and counter electrode Li (JCPDS No. 89-4087) showed typical diffraction peaks. Those at $2\theta = 21°$ agreed with the SEI film and other components (Fig. 6a) [58]. The charge/discharge curves of $CoNiSe_2$/C, corresponding with *In-situ* XRD pattern, covered five parts, including insertion, insertion, conversion, reverse conversion and de-insertion (Fig. 6b). The characteristic diffraction peaks of $CoNiSe_2$ (PDF #65-7038) gradually disappeared when discharged to 1.4 V. The diffraction peaks of $CoNiSe_2$/C at $2\theta = 33.1°$, 44.6° and 50.3° also disappeared, accompanied by the appearance of the diffraction peaks of Ni, Co and $LiSe_2$ (Fig. 6c). The emerging peak at $2\theta = 25.6°$ was related the formation of Li_2Se. The ever-present peak at $2\theta = 45.5°$ during discharge corresponded with the crystal plane of Ni (PDF #88-2326) and Co (PDF #89-7093). These results further confirmed Eq. 1. However, no obvious peak change occurred during charge because of the formation of amorphous $CoNiSe_2$ during reverse conversion process. As a result, the Li storage mechanism of $CoNiSe_2$/C agreed with the redox reaction in CV analysis.

Fig. 7 showed the kinetic analysis of $CoNiSe_2$/C, NiSe/C and $CoSe_2$/C composites. The unchanged size of CV curves for three composites suggested their stable redox reactions (Figs. 7a–c). The intensity and width of redox peaks increased as the scan rate increased from 0.1 to 0.9 mV/s due to the inadequate reaction of electrodes with quickly inserted/de-inserted Li^+ ions [59]. The existing polarization also made redox peaks shift to higher positions. The time-capacity relationship of $CoNiSe_2$/C composite was shown in Fig. 7d. After discharging for 405.5 min, $CoNiSe_2$/C obtained a discharge capacity of 672.6 mAh/g. Such higher discharge suggested the existence of pseudocapacitance contribution. Its Trasatti analysis was calculated by Eqs. 4 and 5. The capacitance-storage capacity ($Q_{capacitive}$) and charge-storage capacity (Q_{total}) relationship of $CoNiSe_2$/C were shown in Figs. 7e and f. The calculated $Q_{capacitive}$ contribution ratio reached up to 52.9%. It was the reason for its excellent electrochemical performance, and also indicated the existence of pseudocapacitance contribution.

$$Q(v) = Q_{capacitive} + \alpha v^{-1/2} \quad (4)$$

$$1/Q(v) = 1/Q_{total} + \alpha v^{1/2} \quad (5)$$

The pseudocapacitance behavior of $CoNiSe_2$/C, NiSe/C and $CoSe_2$/C composites was analyzed by Eqs. 6 and 7 where a, b are the constants and i, v are the current of main peak and the scan rate. The b value between 0.5 and 1 represents that diffusion and pseudocapacitance control the reaction process; the b value equal to 0.5 or 1 represents that the reaction process is controlled by diffusion or pseudocapacitance [60]. The $\log(i)$-$\log(v)$ plots in Fig. 7g showed that the b values of peak1/peak2 for $CoNiSe_2$/C, NiSe/C and $CoSe_2$/C were 0.60/0.74, 0.60/0.73 and 0.76/0.51. The pseudocapacitance-predominant behavior ($k_1 v$) and diffusion-controlled process ($k_2 v^{1/2}$) is quantitatively caculated by Eqs. 8 and 9, wherein k_1 and k_2 are constants. The $i/v^{1/2}$-$v^{1/2}$ plots of three composites at different redox potentials was shown in Figs. S7a–c. The pseudocapacitance contribution ratio was calculated by the equation of $k_1/(k_1 + k_2)$, where k_1 is slope and k_2 is intercept [61]. At 0.5 mV/s, the value was 81.3% for 81.3% $CoNiSe_2$/C (Fig. 7h). The values for three composites at 0.1, 0.3, 0.5, 0.7 and 0.9 mV/s were shown in Fig. 7i. The values increased as the scan rate increased. However, $CoNiSe_2$/C composite still maintained higher values at all scan rates because of its large specific area, excellent conductivity and superior structure stability [62].

$$i = av^b \quad (6)$$

$$\log(i) = b\log(v) + \log(a) \quad (7)$$

$$i = k_1 + k_2 v^{1/2} \quad (8)$$

$$i/v^{1/2} = k_1 v^{1/2} + k_2 \quad (9)$$

Figs. 7j–l showed the *ex-situ* CV tests at 0.5 A/g for $CoNiSe_2$/C, NiSe/C and $CoSe_2$/C composites. All the CV curves gradually tended to become smooth like capacitors under the control of adsorbed redox reaction with the cycles increasing, further making it clear that the existing pseudocapacitance behavior resulted in the increased capacity during cycle [63]. Fig. 7m showed the EIS results of three composites including the pristine Nyquist plots and fitting curves: the semicircle at high frequency region referring to the charge transfer resistance (R_{ct}) and the solid electrolyte interface layer resistance (R_{SEI}), and the line at low frequency oblique referring to the Warburg impedance (W_s). The R_{ct} values for $CoNiSe_2$/C, NiSe/C and $CoSe_2$/C composites were 321, 364 and 446 Ω. The exchange current density for them were 3.9×10^{-2}, 3.5×10^{-2} and 2.8×10^{-2} mA/cm^2 according to Eq. 10 resulting from Butler-Volmer equation. Lower resistance and higher exchange current density were beneficial to accelerating the insertion/de-insertion speed of Li^+ during cycle. Fig. 7n showed the Bode plot of three composites. The most maximum phase angles for $CoNiSe_2$/C, NiSe/C and $CoSe_2$/C were 68.6°, 67.2° and 56.8°, and the τ ($\tau = 1/f$) for them were 0.39, 0.58 and 1.02. As a result, $CoNiSe_2$/C displayed higher capacitive storage capacity than NiSe/C and $CoSe_2$/C. The *ex-situ* EIS results of three composites after circulating 30 cycles were shown in Fig. 7o. $CoNiSe_2$/C still had a lower transfer impedance (132 Ω) than NiSe/C (190 Ω) and $CoSe_2$/C (198 Ω), reflecting its excellent electrochemical performance.

$$i_0 = RT/(nAFR_{ct}) \quad (10)$$

In summary, a bimetallic $CoNiSe_2$/C composite was synthesized and showed superior physical and electrochemical properties in LIBs, enabling it to become a promising anode material. $CoNiSe_2$/C composite had characteristic features such as controllable nanosphere structure, ideal capacity storage, lower transfer resistance and higher pseudocapacitance contribution ratio. At

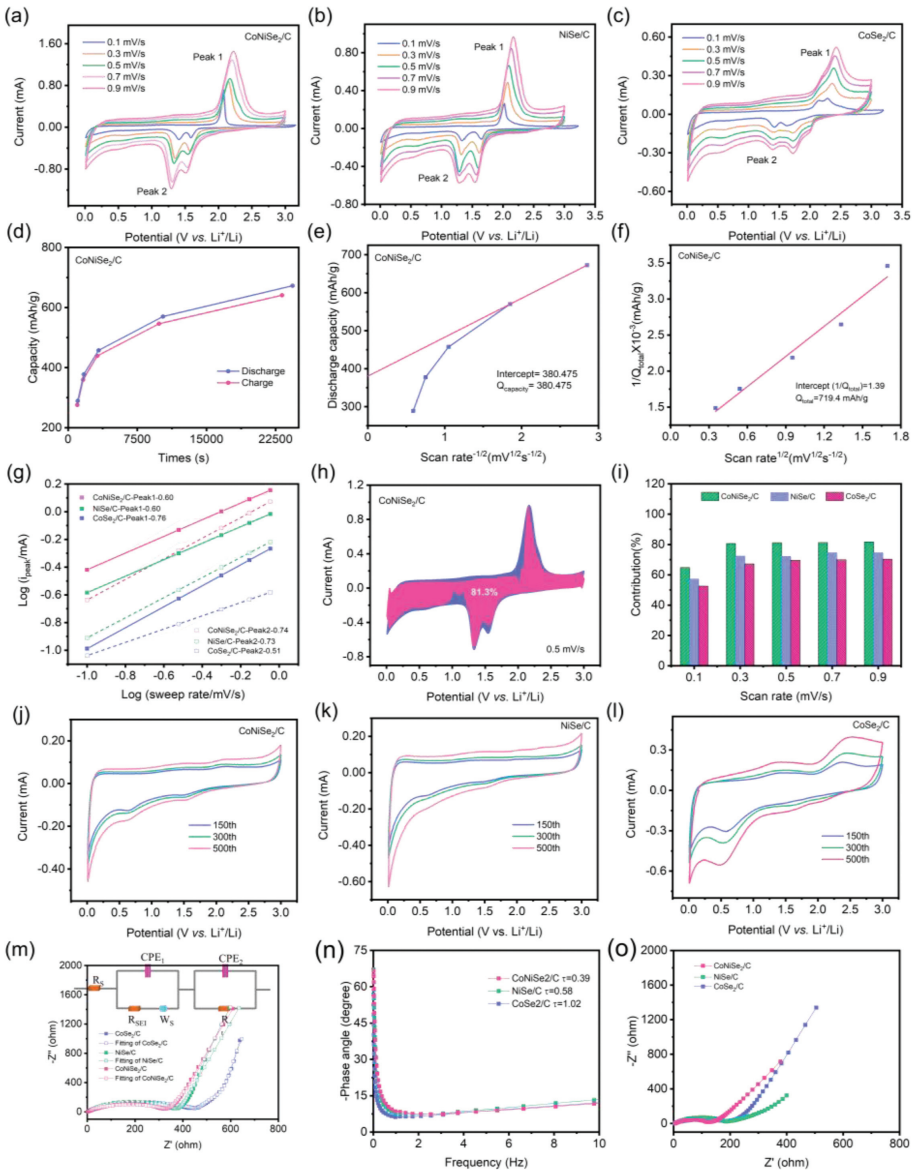

Fig. 7. (a–c) CV curves of $CoNiSe_2$/C, NiSe/C and $CoSe_2$/C at a sweep rate of 0.1–0.9 mV/s. (d–f) Relationship between charge/discharge capacity and time, discharge capacity and $v^{-1/2}$, $1/Q_{total}$ and $v^{1/2}$ of $CoNiSe_2$/C. (g) Relationship between log(i) and log(v) of three composites. (h) Pseudocapacitance control contribution (red) at 0.5 mV/s in the total capacity contribution (blue). (i) Comparison of the *pseudo*-capacitance contribution ratio of three composites at different scanning speeds; (j–l) *Ex-situ* CV curves of $CoNiSe_2$/C, NiSe/C and $CoSe_2$/C at 150th, 300th and 500th cycle at 0.5 A/g. (m) Nyquist diagram and equivalent circuit of three composites under open circuit voltage and after fitting; (n, o) Bode plot and EIS spectra of three composites after circulating 30 cycles at 0.1 A/g.

0.1 A/g circulating for 100 cycles, $CoNiSe_2$/C anodes obtained reversible discharge capacities of 850.9 mAh/g. This study rested on Ni-Co-MOF precursor lays a solid foundation and makes great contribution to the long-term development prospect of new power energy.

Declaration of competing interest

The authors declare that they have no known competing financial interests or personal relationships that could have appeared to influence the work reported in this paper.

Acknowledgments

This work was supported by National Natural Science Foundation, China (Nos. 52071132, 21773057 and U1904216), Zhongyuan Thousand People Plan-The Zhongyuan Youth Talent Support Program (in Science and Technology), China (No. ZYQR201810139), Innovative Funds Plan of Henan University of Technology, China (No. 2020ZKCJ04), and Fundamental Research Funds for the Henan Provincial Colleges and Universities in Henan University of Technology, China (No. 2018RCJH01).

Supplementary materials

Supplementary material associated with this article can be found, in the online version, at doi:10.1016/j.cclet.2022.03.051.

References

[1] Z.Z. Chen, J.G. Hou, J. Zhou, et al., Rare Met. 40 (2021) 3185–3194.
[2] D. Wang, K.H. Tian, J. Wang, et al., Rare Met. 40 (2021) 2464–2473.
[3] Z. Liang, R. Zhao, T. Qiu, et al., EnergyChem 1 (2019) 100001.
[4] C.L. Ma, Z.H. Hu, N.J. Song, et al., Rare Met. 40 (2021) 837–847.
[5] X. Ma, Z.J. Zhang, J.M. Wang, et al., Rare Met. 40 (2021) 2802–2809.
[6] M. Yan, W. Wang, Y. Yin, et al., EnergyChem 1 (2019) 100002.
[7] L.M. Zhu, G.C. Ding, Q. Han, et al., Rare Met. 41 (2022) 425–437.

[8] W. Kang, Y. Zhang, L. Fan, et al., ACS Appl. Mater. Interfaces 9 (2017) 10602–10609.
[9] Y. Huang, X. Zhu, D. Cai, et al., J. Energy Chem. 59 (2021) 473–481.
[10] C. Huang, A. Gao, F. Yi, et al., Chem. Eng. J. 419 (2021) 129643.
[11] C. Xu, C. Jin, J. Liu, et al., J. Energy Storage 36 (2021) 102394.
[12] X. Wang, H. Qiu, H. Liu, et al., Green Chem. 20 (2018) 4901–4910.
[13] C. Li, T. Chen, W. Xu, et al., J. Mater. Chem. A 3 (2015) 5585–5591.
[14] J. Liu, R. Xu, C. Yan, et al., Energy Storage Mater. 30 (2020) 27–33.
[15] M. Zhang, R. Liu, Z. Wang, et al., Chin. Chem. Lett. 31 (2020) 1217–1220.
[16] J. Hao, X. Xu, H. You, et al., Chem. Eng. J. 418 (2021) 129475.
[17] R. Zhang, Z. Xue, J. Qin, et al., J. Energy Chem. 50 (2020) 143–153.
[18] C. Sun, M. Liu, L. Wang, et al., Chin. Chem. Lett. 33 (2022) 1779–1797.
[19] L. Li, J. Zhao, Y. Zhu, et al., Electrochim. Acta 353 (2020) 136532.
[20] P. Ge, S. Li, L. Xu, et al., Adv. Energy Mater. 9 (2019) 1803035.
[21] J. Liu, H. Yuan, H. Liu, et al., Adv. Energy Mater. (2021) 2100748.
[22] W. Sun, C. Cai, X. Tang, et al., Chem. Eng. J. 351 (2018) 169–176.
[23] Z. Zhang, X. Shi, X. Yang, et al., ACS Appl. Mater. Interfaces 8 (2016) 13849–13856.
[24] L.Q. Zhang, C.X. Zhu, S.C. Yu, et al., J. Energy Chem. 66 (2022) 260–294.
[25] L. Wang, Z. Wang, L. Xie, et al., Electrochim. Acta 343 (2020) 136138.
[26] Q. Wang, X. Ran, W. Shao, et al., J. Power Sources 490 (2021) 229517.
[27] W. Sun, Y. Zhang, Y. Wang, ChemElectroChem 6 (2019) 3736–3741.
[28] J. Li, D. Yan, T. Lu, et al., Chem. Eng. J. 325 (2017) 14–24.
[29] T. Yang, Y. Liu, D. Yang, et al., Energy Storage Mater. 17 (2019) 374–384.
[30] Y. Li, Y. Xu, Z. Wang, et al., Adv. Energy Mater. 8 (2018) 1800927.
[31] T. Lu, S. Dong, C. Zhang, et al., Coord. Chem. Rev. 332 (2017) 75–99.
[32] G. Fang, Q. Wang, J. Zhou, et al., ACS Nano 13 (2019) 5635–5645.
[33] G. Xu, P. Nie, H. Dou, et al., Mater. Today 20 (2017) 191–209.
[34] Y. Zhao, Z. Song, X. Li, et al., Energy Storage Mater. 2 (2016) 35–62.
[35] J.W.M. Osterrieth, D. Fairen-Jimenez, Biotechnol. J. 16 (2021) 2000005.
[36] F. Xiao, H. Wang, T. Yao, et al., ACS Appl. Mater. Interfaces 13 (2021) 18010–18020.
[37] S. Sung, B.H. Kim, S. Lee, et al., J. Energy Chem. 60 (2021) 186–193.
[38] Y. Han, P. Qi, J. Zhou, et al., ACS Appl. Mater. Interfaces 7 (2015) 26608–26613.
[39] Z. Zhao, S. Wang, R. Liang, et al., J. Mater. Chem. A 2 (2014) 13509–13512.
[40] G. Xu, Y. Zuo, B. Huang, J. Electroanal. Chem. 830-831 (2018) 43–49.
[41] L. Wang, P. Gao, D. Bao, et al., Cryst. Growth Des. 14 (2014) 569–575.
[42] D. Zhu, F. Zheng, S. Xu, et al., Dalton Trans. 44 (2015) 16946–16952.
[43] C.V.V. Muralee Gopi, A.E. Reddy, H.J. Kim, J. Mater. Chem. A 6 (2018) 7439–7448.
[44] W. Lu, M. Liu, L. Miao, et al., Electrochim. Acta 205 (2016) 132–141.
[45] G. Ćirić-Marjanović, I. Pašti, N. Gavrilov, et al., Chem. Pap. 67 (2013) 781–813.
[46] Y.B. Yin, J.J. Xu, Q.C. Liu, X.B. Zhang, Adv. Mater. 28 (2016) 7494–7500.
[47] Q. Tan, W. Zhao, K. Han, et al., J. Mater. Chem. A 7 (2019) 15673–15682.
[48] L. Wang, Z. Wang, L. Xie, et al., ACS Appl. Mater. Interfaces 11 (2019) 16619–16628.
[49] X. Wang, Y. Li, J. Mater. Chem. A 4 (2016) 5247–5257.
[50] X. Wu, Z. Shi, L. Zou, et al., J. Power Sources 378 (2018) 119–124.
[51] M.C. Biesinger, B.P. Payne, A.P. Grosvenor, et al., Appl. Surf. Sci. 257 (2011) 2717–2730.
[52] G.D. Park, Y.C. Kang, Chem. Eur. J. 22 (2016) 4140–4146.
[53] X. Sun, G. Hao, X. Lu, et al., J. Mater. Chem. A 4 (2016) 10166–10173.
[54] X. Zhu, S. Li, J. Li, et al., Electrochim. Acta 295 (2019) 22–28.
[55] Z. Zhang, X. Shi, X. Yang, Electrochim. Acta 208 (2016) 238–243.
[56] F. Fu, J. Li, Y. Yao, et al., ACS Appl. Mater. Interfaces 9 (2017) 16194–16201.
[57] C. Ye, Y. Jiao, D. Chao, et al., Adv. Mater. 32 (2020) 1907557–1907578.
[58] L. Wang, L. Zhu, W. Zhang, et al., J. Colloid Interface Sci. 586 (2021) 730–740.
[59] S. Sharafzadeh, A. Nezamzadeh-Ejhieh, Electrochim. Acta 184 (2015) 371–380.
[60] L. Zhu, Q. Sun, L. Xie, X. Cao, Int. J. Energy Res. 44 (2020) 4586–4594.
[61] D. Cao, W. Kang, S. Wang, et al., J. Mater. Chem. A 7 (2019) 8268–8276.
[62] J. Li, D. Yan, S. Hou, et al., Chem. Eng. J. 335 (2018) 579–589.
[63] H.S. Jadhav, G.M. Thorat, J. Mun, J.G. Seo, J. Power Sources 302 (2016) 13–21.